scientific reports

Check for updates

OPEN

Transverse force sensing with a uniform FBG and unpolarized light via machine learning

Victor Tocanne[1], Bastien Van Esbeen[2]✉, Damien Kinet[1], Corentin Guyot[1] & Christophe Caucheteur[2]

In this paper, we report that a uniform fiber Bragg grating (FBG), interrogated with broadband light, can be used to reliably measure transverse force through the analysis of its unpolarized reflected amplitude spectrum. Unlike conventional FBG-based transverse force sensors, which typically rely on birefringence-induced spectral splitting or polarization-resolved interrogation schemes, our approach leverages the full spectral shape of the reflected signal, recorded with standard illumination. Two types of measurement devices are used for the readout process: (i) a broadband light source combined with an optical spectrum analyzer, and (ii) a spectrometer-based FBG interrogator. Both approaches yield similar performance in controlled conditions, confirming the robustness of the FBG interrogator, which is the only configuration suitable for deployment in the field. By training a model with hundreds of experimental spectra measured for calibrated transverse force values between 0 and 70 N, we achieve highly accurate and robust prediction of the applied transverse force, with a mean absolute error of 2.80 N for the multilayer perceptron (MLP) and 0.44 N for the gradient boosting (XGBoost) model. This data-driven method removes the need for polarization control or complex grating structures, and opens a new pathway towards simple, cost-effective, and highly sensitive transverse force sensing.

Keywords Fiber bragg gratings, Transverse sensing, Machine learning, Birefringence, Unpolarized measurement

Fiber Bragg gratings (FBGs) are well-established optical sensors for temperature and strain monitoring due to their small size, multiplexing capabilities, and immunity to electromagnetic interference, among other unique assets[1]. Measuring one of these two quantities is rather straightforward as the information is encoded into a Bragg wavelength shift that is easy to finely track from the reflected amplitude spectrum measurement. However, the measurement of transverse forces using FBGs remains considerably more challenging, as the response involves stress-induced birefringence rather than a wavelength shift[2]. Accurately measuring transverse force with FBGs usually relies on sensing stress-induced birefringence, which causes the Bragg reflection to split into two polarization-dependent resonances[2–6]. Indeed, when a transverse load is applied to an optical fiber, it breaks the symmetry of the fiber's cross-section. This disruption introduces local birefringence, causing the two orthogonal polarization modes (or eigenmodes) to lose their degeneracy. If an FBG is located where the load is applied, this birefringence leads to two distinct reflection peaks, separated in wavelength by an amount that depends on the load's magnitude. If the wavelength separation exceeds the width of the reflection band, the two reflection peaks become clearly resolved, enabling straightforward measurement of the load. However, for relatively small lineic loads (typically below 1 N/mm), this splitting does not produce a discernible effect on the amplitude spectrum. This limitation can be mitigated by using an FBG written in a polarization-maintaining fiber (PMF)[7–10] or a π-phase-shifted FBG[11], both of which allow the amplitude response to remain sensitive to the applied load. Alternatively, it has been shown that the spectral characteristics of polarization-dependent loss (PDL), differential group delay (DGD) or Stokes parameters are highly responsive to birefringence[12–15]. As a result, such measurements provide an effective means to detect and quantify weak transverse loads, but at the cost of requiring control of the input state of polarization or the use of rather complex interrogation devices, which are not well suited for operation outside of laboratory settings. More recently, the use of FBGs encapsulated in a polymer matrix has proven effective for transverse force measurement[16]– [17], although this comes at the expense of the simplicity and advantages offered by bare FBGs.

[1]B-SENS SRL, Boulevard Dolez 31, Mons 7000, Belgium. [2]Advanced Photonic Sensors Unit, Department of Electromagnetism and Telecommunication, University of Mons, Mons 7000, Belgium. ✉email: bastien.vanesbeen@umons.ac.be

Beyond laboratory demonstrations, transverse force sensing with FBGs has important applications across several domains[18]. In structural health monitoring, FBGs can detect local pressures within materials in which they are embedded, enabling the identification of stress concentrations or delamination zones[19]. In aerospace and wind energy, they can monitor bearing loads, bonding integrity, or composite layer compression[20]. In biomechanics and robotics, FBG-based tactile or pressure sensors are increasingly used to quantify contact forces in prosthetics or soft grippers[21]. In civil engineering, such sensors can measure contact forces in cables, supports, or joints, while in railway or tire monitoring, they enable the assessment of wheel-rail or tire-road interactions[22]. Despite this wide range of potential uses, most existing FBG-based force sensors remain difficult to deploy due to their polarization dependence, sensitivity to alignment, or reliance on custom grating designs.

In parallel, machine learning has recently emerged as a powerful tool for extracting subtle information from optical spectra. Supervised models such as neural networks and gradient boosting have been successfully applied to predict parameters such as temperature[23], strain[24], shape[25], refractive index[26–27], or chemical concentration[28] from the spectral response of FBGs. By learning relationships between spectral features and physical quantities, machine learning enables accurate inference even when analytical models are unavailable or impractical.

In this work, we introduce a novel FBG-based transverse force sensing technique that overcomes the aforementioned limitations by using unpolarized light from an amplified spontaneous emission (ASE) source. As a reference, an optical spectrum analyzer (OSA) is used to provide high spectral resolution. However, the vast majority of the data is acquired using a spectrometer-based FBG interrogator, which offers a coarser nominal wavelength sampling of approximately 170 pm and is more suitable for practical field applications. In both cases, rather than relying on explicit polarization-resolved measurements, we apply machine learning algorithms to interpret the subtle modifications of the spectral shape caused by transverse loading. The relative performance of two machine learning methods (multilayer perceptron (MLP) and XGBoost method, further abbreviated as XGB) is compared in the following. To our knowledge, this is the first demonstration of transverse force sensing that leverages the full amplitude spectrum of the FBG under unpolarized light, enabling accurate force estimation with a simplified and robust interrogation scheme.

Theoretical background

FBGs subject to transverse loading and birefringence

In optical fibers, the birefringence Δn is defined as the difference between the effective refractive indices n_x and n_y of the two orthogonal eigenmodes (*x* and *y*):

$$\Delta n = n_x - n_y \tag{1}$$

When an optical fiber is subjected to a transverse load, the circular symmetry of its cross-section is broken, leading to a strong anisotropy in the refractive index distribution. As a result, the effective refractive indices of the eigenmodes become very different from each other. This stress-induced birefringence is proportional to the transverse force *F* applied to a fiber length *L*[29]:

$$\Delta n = -\frac{4n^3\,(1+\nu\,)}{\pi\,E}\,(p_{11}-p_{12})\cdot\left(\frac{F}{DL}\right) \tag{2}$$

where p_{11} and p_{12} are the Pockels photoelastic coefficients, *E* and *v* the Young's modulus and Poisson's ratio of silica, respectively, *D* is the fiber diameter, and *n* the core refractive index.

MLP and XGB machine learning algorithms

This section provides some basic information about the two machine learning methods that were implemented in this work.

MLP is a feedforward neural network composed of successive layers of artificial neurons. Each neuron applies a nonlinear transformation to the input data, allowing the network to approximate complex relationships between variables. In the context of FBG sensing[30], the MLP can learn how the reflected spectral shape varies with the applied transverse force. Through an iterative training process using labeled data, the model adjusts its internal parameters to minimize prediction errors. Once trained, the MLP can infer the applied force from new spectral measurements by exploiting the nonlinear correlations encoded in the spectrum.

XGB algorithm belongs to the family of ensemble methods based on decision trees. It constructs multiple shallow trees in sequence, where each tree focuses on correcting the residual errors of the previous ones. This boosting strategy enables the model to capture subtle, localized patterns in the spectral data while maintaining strong generalization performance. Because of its robustness to noise, its ability to handle high-dimensional inputs, and its built-in regularization mechanisms, XGB is particularly well-suited to the analysis of complex optical spectra such as those produced by FBG sensors under mechanical loading[31].

Experiments

FBGs used in this work were inscribed in photosensitive single-mode optical fibers (type PS1550 from Fibercore) using the NORIA system (Northlab Photonics) comprising a 193 nm excimer laser and a rotation stage that can host up to 16 phase masks. The gratings were 4 mm long and were inscribed with only 500 pulses of 5 mJ, ensuring that the photo-induced birefringence remains below 10^{-6}, so that its effect can be considered negligible with respect to the applied transverse force.

For transverse strain sensing, the FBGs were integrated into the setup depicted in Fig. 1, where the applied force is exerted at the center of a specifically designed mechanical piece (dimensions: $100\times50\times20$ mm^3, weight: 360 g). This piece, machined from anodized aluminum, contains two parallel sections where two optical fibers

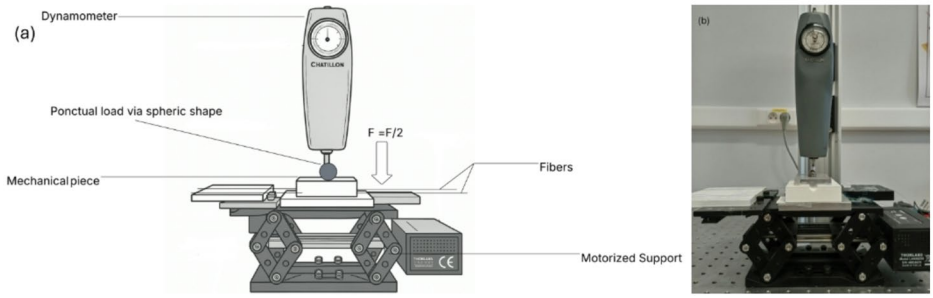

Fig. 1. Experimental setup used to apply controlled transverse force to a uniform FBG: (**a**) sketch, and (**b**) picture of the actual setup.

can be placed: the sensing fiber containing the FBG, on the one hand, and an identical dummy fiber, on the other hand. The dummy fiber serves to balance the mechanical stress on both sides of the loading plate, preventing unwanted tilt or bending of the block and ensuring that the applied force remains purely transverse to the fiber axes. The force experienced by the FBG (F_{FBG}) is equal to the ratio of the FBG length (L_{FBG}) over the fiber length under load (L_{load}), times half (because of the presence of the dummy fiber) the total applied force (F_{app}). It corresponds to the following relationship:

$$F_{\mathrm{FBG}} = \frac{L_{\mathrm{FBG}}}{L_{\mathrm{load}}} \frac{1}{2} F_{\mathrm{app}} \tag{3}$$

The force is applied by moving up the support via a motorized vertical-axis translation stage and its value is measured by an analog Chatillon DPP-10 force gauge.

To measure the reflected amplitude spectrum of the FBG under test, two measurement setups were employed. The first, used as a reference, consisted of an unpolarized ASE broadband optical source (Amonics ALS-CL-17-B-FA) combined with an optical spectrum analyzer (OSA, Yokogawa AQ6370B), providing a spectral resolution of 20 pm with a repeatability of ± 5 pm. The second setup, suitable for practical field deployment, utilized the BSI-108 FBG interrogator from B-Sens (hereafter referred to as FBG interrogator), a high-speed, 512-pixel spectrometer-based device. For both configurations, standard optical fiber connectors were used, without any control of the polarization state. During some measurements, the connectors were intentionally shaken to show that the reflected amplitude spectrum remains unaffected, demonstrating its robustness to polarization fluctuations. As stated in the introduction, we aimed to predict the applied transverse force from the shape of the FBG spectrum using machine learning techniques. To this end, a dataset of 1269 spectra was experimentally created based on OSA measurements. This dataset is composed of nine subdatasets containing 141 spectra, each labeled with a known force (read by the dynamometer), taking values from 0 to 70 N in steps of 0.5 N. The spectra were recorded by the OSA with a wavelength span of 4.2 nm centered around the Bragg wavelength and are composed of 501 sampling points. The dataset collected with the FBG interrogator was much more important. It consisted of 7050 spectra divided into 50 subdatasets, with a length span of 86 nm composed of 512 pixels (resolution of ~ 170 pm). Figure 2(a) depicts the reflected amplitude spectrum measured for several load values, confirming the progressive splitting as a function of the increase in the transverse force value, due to the mechanically-induced birefringence. Figure 2(b) shows the reflected amplitude spectra measured for the nine datasets at a transverse force value of 14 N. It confirms the overall good repeatability of the measurements process. It produced a standard deviation below 0.05% on the reflected peak amplitude and below 0.06 nm on the Bragg wavelength. Uncertainty in the applied force stems from the force gauge resolution, which is 0.1 N.

Experimental results

Two different supervised learning models were investigated to compare their relative performance in determining the actual transverse force value from the shape of the reflected amplitude spectrum. They were chosen because of their ability to model complex, nonlinear relationships inherent in spectral data.

To retrieve the applied transverse force from the reflected spectrum, we explored two supervised machine learning models: a multilayer perceptron (MLP) and an extreme gradient boosting (XGB). The MLP is a feedforward neural network composed of successive layers of interconnected nodes, each applying a nonlinear transformation to extract hierarchical features from the input spectral profile. It is well-suited to capture complex, nonlinear relationships between spectral variations and the corresponding force values. In parallel, the XGB regressor builds an ensemble of decision trees (DT) in a sequential way, where each tree attempts to correct the errors made by the previous ones. This gradient-boosting strategy efficiently models intricate dependencies while maintaining good generalization capabilities. Both models were trained on labeled datasets of reflectivity spectra acquired under controlled transverse loading conditions, enabling robust and accurate prediction of the force from subtle spectral distortions induced by the applied stress. The overall method of training and optimization of both models can be found in Fig. 3.

For the MLP, the dataset was split into 90% of train in 8 subdatasets, 10% of validation on those same 8 subdatasets, and the 9th subdataset for testing. The training was performed over a maximum of N_{epoch} = 100

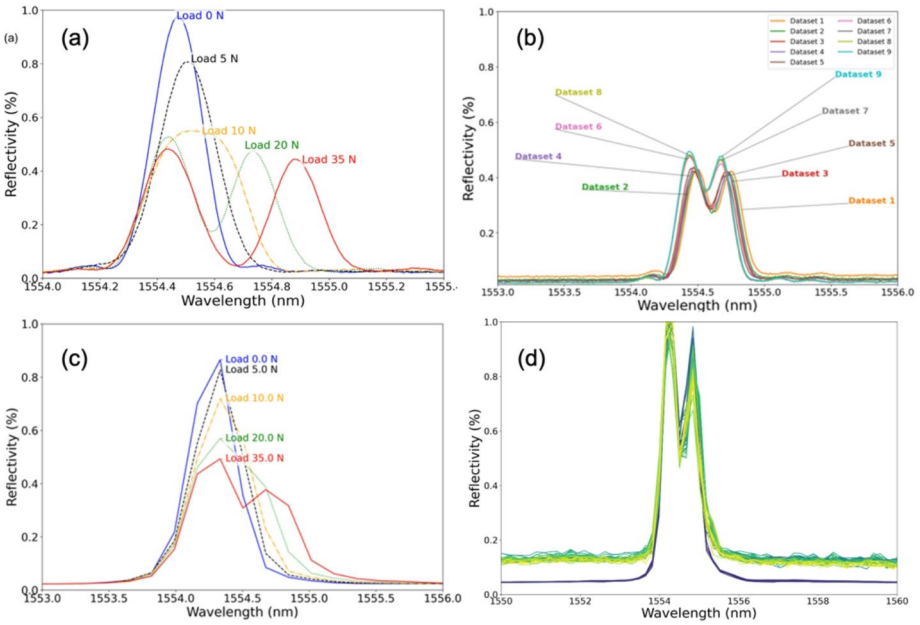

Fig. 2. Reflected amplitude spectrum of a 4 mm long FBG measured with the OSA: (**a**) for different transverse force values of a given subdataset (#9), and (**b**) for the 9 subdatasets at a given force value (14 N). Reflected spectrum measured with the FBG interrogator: (**c**) for different transverse force values of a given subdataset (#9), and (d) for the 50 subdatasets at a given force value (50 N).

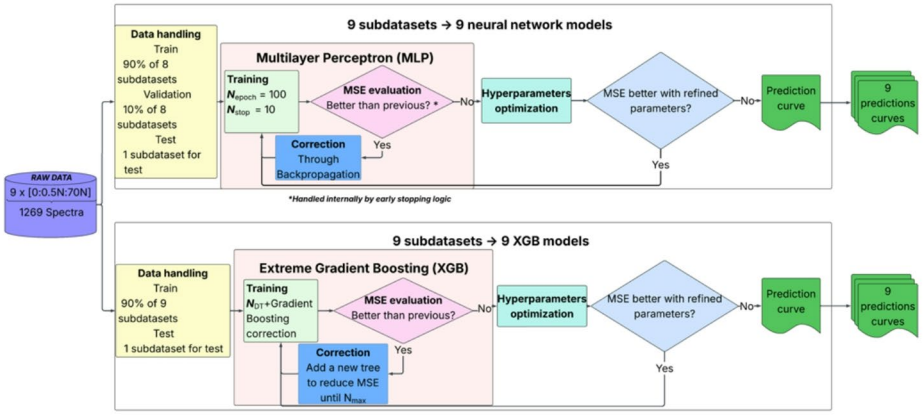

Fig. 3. Flow chart summarizing the operating process of the MLP and XGB methods.

iterations, with an early stopping mechanism triggered if the mean squared error (MSE) evaluation on the validation set failed to improve over N_{stop} = 10 epochs. The MSE is defined as

$$\mathrm{MSE} = (1/n)\sum_{i=1}^{n}(y_i - ?_i)^2 \tag{4}$$

where y_i and $\hat{y}_i$ denote the true and predicted force values, respectively, and n is the number of validation samples. This loss function penalizes large errors more severely due to the squaring term, which helps steer the optimization process to reduce outlier deviations during training. In addition, MSE is differentiable and smooth, which makes it particularly well-suited for gradient-b as ed learning methods such as backpropagation, unlike the mean absolute error (MAE), whose gradient is less stable near zero. For these reasons, MSE was chosen as the criterion for early stopping and model selection.

During each epoch, model correction was applied via backpropagation. Once a candidate model was trained, a hyperparameters optimization step was performed using Optuna[32], exploring architectural parameters such as the number of hidden layers, neurons per layer, activation functions, and learning rate. If the "MSE better with refined parameters?" condition was met, the optimized model was retained. Otherwise, the initial model was

kept, and the corresponding prediction curve was generated. This process was repeated to yield nine predictions curves.

The same procedure, this time for 50 subdatasets, was then applied to the dataset acquired using the FBG interrogator, ensuring a consistent training and optimization framework across both datasets. Model selection and curve generation followed the same performance criterion, enabling direct comparison of the predictive accuracy between the dataset acquired with the OSA and the one obtained with the FBG interrogator.

The selected MLP model (configuration and parameters in Table 1) processes 501 input features through three dense (fully connected) layers interleaved with dropout layers. Dense layers perform weighted combinations of inputs and apply nonlinear activation functions (ReLU here) to learn complex relationships. Dropout layers randomly deactivate a fraction of neurons during training, which reduces overfitting and improves the model's ability to generalize. The final output layer has a single neuron with a linear activation, suitable for continuous value prediction in regression tasks. The model contains 38,561 trainable parameters, which are adjusted during training. Optimization is performed using the Adam optimizer, which adaptively adjusts the learning rate for each parameter based on gradient estimates (β_1 and β_2 control momentum and variance adaptation; ε prevents division by zero). The learning rate (0.001) determines how much the weights are updated in each step. The loss function is the MSE, which penalizes large deviations between predicted and actual values, guiding the optimizer toward better accuracy. Training was conducted on 50 sub-datasets acquired with the FBG interrogator following the same procedure used for the OSA dataset, ensuring that results from both systems can be directly compared.

For the XGB models, the input data were divided into eight subdatasets of training and the remaining subdataset for testing. Each model was built by sequentially adding decision trees: at each step, a new tree was added, attempting to reduce the overall loss through gradient boosting correction. This continued until a predefined number of estimators N_{max} was reached, or until MSE evaluation no longer improved. As with the MLP, an optimization step of the hyperparameters was performed using Optuna, tuning tree depth, learning rate, and number of estimators. The refined model was retained only if it yielded improved performance. The resulting prediction curve was then extracted (nine in total).

This same training, boosting, and optimization procedure was subsequently applied to the dataset acquired using the FBG interrogator. The same model selection criterion ensured that only configurations with improved MSE were retained, allowing a direct and consistent comparison between the predictive outputs from the standard dataset and those from the FBG interrogator-acquired dataset.

The optimal hyperparameters selected through the Optuna optimization process for the retained XGB models were as follows: a learning rate of 0.06347, allowing a gradual yet stable convergence during boosting; 512 estimators (trees) to ensure sufficient model complexity without overfitting; a maximum tree depth of 6, balancing expressiveness and generalization; an L2 regularization term (λ) of 1.97715 to limit overfitting. The objective function was set to *reg: squarederror* for regression tasks, with a fixed random state of 42 to guarantee reproducibility. Computations were restricted to a single CPU thread ($n_{jobs} = 1$) to ensure consistency across runs, and verbosity was disabled for streamlined execution.

The choice of Optuna for hyperparameter tuning was motivated by its efficiency in navigating high-dimensional parameter spaces. In contrast to conventional grid search methods, which exhaustively evaluate all combinations in a predefined grid and become computationally prohibitive as the number of parameters increases, Optuna adopts a more intelligent search strategy. Its use of adaptive sampling (based on Bayesian optimization via a Tree-structured Parzen Estimator) allows it to prioritize promising regions of the search space while discarding suboptimal ones early on. This results in a significantly reduced number of evaluations required to identify well-performing configurations. Given the number of tunable parameters in both MLP (e.g., depth, width, learning rate) and XGB (e.g., tree depth, learning rate, number of estimators), employing grid search would have been prohibitively time-consuming. Optuna enabled us to achieve competitive performance with a manageable computational cost. The latter remained always less than 30 min. Using Optuna for hyperparameter optimization reduces the search cost from $O(n^4)$ to $O(n_{trials})$, with $n_{trials} << n^4$, enabling efficient exploration of high-dimensional spaces. Unlike grid-search method, it intelligently selects promising configurations without exhaustive evaluation.

To assess the generalization capabilities of both models, we adopted a leave-one-dataset-out strategy over the nine available subdatasets. Each subdataset was excluded once to serve as a test set, while the remaining eight were used for training and validation. This cross-validation scheme, performed independently for both the MLP and XGB models, ensured a fair evaluation of predictive performance across unseen spectral profiles. The final comparison focuses on the test set corresponding to subdataset 9, which was excluded entirely from the model training phase.

Figure 4 displays the predicted versus true transverse force values for both read out devices and both models, with the red line indicating perfect prediction. Blue circles correspond to the MLP predictions, while green crosses denote those of the XGB regressor. The inset bar plot shows the global MAE computed across all folds, with

Input	501 features
Architecture	Dense (64, ReLU) → Dropout → Dense (32, ReLU) → Dropout → Dense (128, ReLU) → Dropout → Dense (1, Linear)
Number of trainable parameters	38,561
Optimizer	Adam (LR = 0.001; $\beta_1 = 0.9$; $\beta_2 = 0.999$; $\varepsilon = 1 \times 10^{-7}$)
Loss function	MSE

Table 1. Optimal MLP model configuration and parameters.

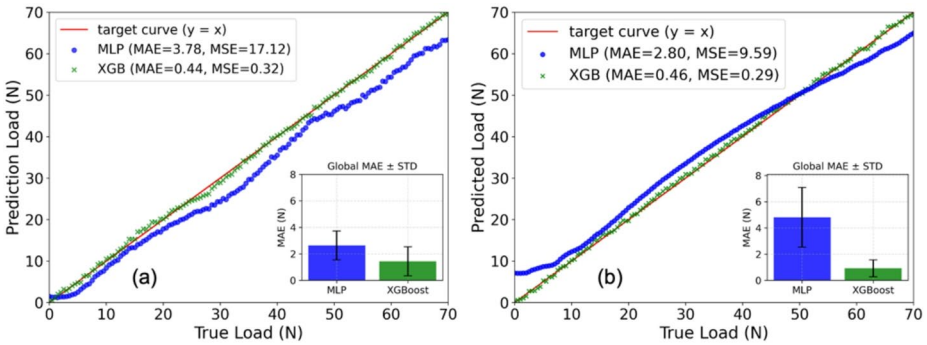

Fig. 4. Typical results confirming the performance of the MLP and XGB methods in predicting the transverse force value from the shape of the FBG reflected amplitude spectrum. Inset: average and standard deviation of the MSE for both methods, computed from the nine iterations. (**a**) Measurements with the OSA, (**b**) measurements with the BSI-108 interrogator.

error bars representing the standard deviation (STD). For the OSA measurements (Fig. 4(a)), XGB outperforms MLP in terms of MAE (0.44 N vs. 3.78 N), and also slightly in terms of consistency (STD of 1.10 N vs. 1.44 N). Figure 4(b) shows that, in the high-data regime provided by the FBG interrogator (50 measurements per fold), the XGB regressor not only outperforms the MLP, but it does also so by a wide margin in both accuracy and consistency. XGB achieves an MAE of 0.46 N and an MSE of 0.29 N^2, whereas the MLP remains at substantially higher error levels (MAE = 2.80 N, MSE = 9.59 N^2) under the same conditions. Beyond delivering lower absolute error, XGB also exhibits markedly tighter prediction spread around the target, indicating highly repeatable behavior. This performance gap reflects the ability of gradient boosting to iteratively correct residuals across many weak learners, allowing it to exploit subtle spectral nonlinearities and noise structure that the MLP does not capture effectively. Under realistic interrogator sampling, XGB provides both lower force estimation error and far more reliable predictions than the MLP, establishing it as the superior model for transverse force sensing.

The determination coefficients further confirm the excellent agreement between predicted and measured forces. For the OSA dataset (Fig. 4(a)), the MLP and XGB models achieved R^2=0.959 and R^2=0.999, respectively, while for the FBG interrogator dataset (Fig. 4(b)), the corresponding values reached R^2=0.977 and R^2=0.999. These high coefficients demonstrate that both models capture almost all the variance in the experimental data, with XGB providing an almost perfect fit to the reference measurements. The slightly lower R^2 of the MLP mainly arises from small deviations observed at low transverse forces, highlighting the superior ability of the gradient-boosting approach to model fine nonlinear spectral variations.

Compared to conventional FBG-based force sensing techniques that rely on clearly resolved birefringence-induced peak splitting, the machine-learning-based approach leverages the full amplitude spectrum to infer the applied force. This enables the detection of slight spectral distortions that are typically inaccessible through analytical or peak-tracking methods. As a result, the proposed method provides accurate force estimation even in the low-load regime, where traditional birefringence analysis fails. Furthermore, the data-driven nature of the models eliminates the need for complex calibration procedures or customized grating structures, making the system simpler and more suitable for field deployment.

Conclusions

In this work, we proposed and experimentally validated a simple and cost-effective approach for transverse force sensing using a uniform fiber Bragg grating interrogated with broadband light. Instead of relying on polarization control or complex grating geometries, we exploited the full reflected amplitude spectrum and processed it with machine learning models to extract accurate predictions of the applied force. This strategy leverages the information-rich spectral response of the grating, while at the same time simplifying the optical interrogation system.

We designed a comprehensive dataset acquisition protocol, collecting hundreds of experimental spectra over a calibrated transverse force range of 0–70 N. Two distinct acquisition systems were used, namely an OSA-based setup and an FBG interrogator, in order to validate the robustness of the method across different hardware platforms. Multiple models were trained and optimized, with particular attention given to multilayer perceptron (MLP) and gradient boosting (XGB). The performance of the models was carefully evaluated using mean absolute error, mean squared error, and mean relative error as benchmarks.

Machine learning, and particularly gradient boosting methods, have proven highly effective in extracting subtle information from spectral profiles that would otherwise remain inaccessible with traditional signal processing techniques. The excellent accuracy achieved by XGB compared to MLP further underlines the importance of model selection and optimization when dealing with high-dimensional spectral datasets.

Data availability

All data are available upon reasonable request to the corresponding author.

Received: 23 September 2025; Accepted: 10 November 2025

Published online: 24 December 2025

References

1. Hill, K. & Meltz, G. Fiber Bragg grating technology fundamentals and overview. *J. Lightwave Technol.* **15**, 1263–1276 (1997).
2. Barlow, A. J. & Payne, D. N. The stress-optic effect in optical fibers. *IEEE J. Quantum Electron.* **19**, 834–839 (1983).
3. Gafsi, R. & El-Sherif, M. Analysis of induced-birefringence effects on fiber Bragg gratings. *Opt. Fiber Technol.* **6**, 299–323 (2000).
4. Espejo, R. J. & Dyer, S. D. Transverse-stress fiber Bragg grating sensor with high Spatial resolution and temperature stability. *J. Lightwave Technol.* **25**, 1777–1785 (2007).
5. Caucheteur, C., Guo, T. & Albert, J. Polarization-assisted fiber Bragg grating sensors: tutorial and review. *J. Lightwave Technol.* **35**, 3311–3322 (2017).
6. Xiong, J. et al. Spectral splitting sensing using optical fiber Bragg grating for spacecraft lateral stress health monitoring. *Appl. Sci.* **13**, 4161 (2023).
7. Udd, E. Review of multi-parameter fiber grating sensors. *Proc. SPIE* **6770**, 677002 (2007).
8. Gouws, A., Ford, K. R. & Jones, B. H. Transverse strain measurements in polymer-embedded, polarization-maintaining fiber Bragg gratings. *Eng. Res. Express*. **2**, 045016 (2022).
9. Wachtarczyk, K. et al. In-plane strain measurement in composite structures with fiber Bragg grating written in side-hole elliptical core optical fiber. *Materials* **15**, 77 (2022).
10. Geernaert, T. et al. Transverse load sensing with fiber Bragg gratings in microstructured optical fibers. *IEEE Photon Technol. Lett.* **21**, 6–8 (2009).
11. LeBlanc, M. et al. Transverse load sensing by use of pi-phase-shifted fiber Bragg gratings. *Opt. Lett.* **24** (16), 1091–1093 (1999).
12. Caucheteur, C. et al. Transverse strain measurements using the birefringence effect in fiber Bragg gratings. *IEEE Photon Technol. Lett.* **19**, 966–968 (2007).
13. Wang, Y., Wang, M. & Huang, X. High-sensitivity fiber Bragg grating transverse force sensor based on centroid measurement of polarization-dependent loss. *Meas. Sci. Technol.* **21**, 065304 (2010).
14. Descamps, F. et al. Distribution profiling of a transverse load using the DGD spectrum of chirped FBGs. *Opt. Express*. **23**, 18203–18217 (2015).
15. Su, Y. et al. Real-time transverse force sensing using fiber Bragg grating through direct Stokes parameters measurement. *Opt. Express*. **23**, 32300–32310 (2015).
16. Vicente, J. L. M. et al. Study of the transverse strain effect on the fiber Bragg grating sensors (FBGS) response with polyimide coating under experimental biaxial tests. *Compos. Struct.* **326**, 117621 (2023).
17. Gonzalez-Gallego, M. Fiber Bragg gratings sensor strain-optic behavior with different polymeric coatings subjected to transverse strain. *Polymers* **16**, 1223 (2024).
18. Mizutani, T. et al. Influence of stress induced birefringence on FBG senors embedded in CFRP laminates. *Proc. Fourth Asian-Australasian Conference on Composite Materials* 937–942 (2014).
19. Güemes, J. A. et al. "Embedded fiber Bragg grating as local damage sensors for composite materials," *Proc. SPIE* **4694**, 118–128 (2002).
20. Liang, Q., Zou, K., Long, J., Jin, J., Zhang, D., Coppola, G., Sun, W., Wang, Y. & Ge, Y. Multi-component FBG-based force sensing systems by comparison with other sensing technologies: A review. *IEEE Sens. J.* **18**(18), 7345–7357 (2018). https://doi.org/10.1109/JSEN.2018.2861014
21. Neto, V. B., Marques, C., Frizera-Neto, A. & Leal-Junior, A. G., FBG-based sensing system to improve tactile sensitivity of robotic manipulators working in unstructured environments. *Sens. Actuators A: Phys.* **359**, 114473 (2023). https://doi.org/10.1016/j.sna.2023.114473
22. Yassin, M. H., Farhat, M. H., Soleimanpour, R. & Nahas, M. Fiber Bragg grating (FBG)-based sensors: A review of technology and recent applications in structural health monitoring (SHM) of civil engineering structures. Discov. Civ. Eng. **1**(1), 151 (2024). https://doi.org/10.1007/s44290-024-00141-4
23. Djurhuus, M. S. E. et al. Machine learning assisted fiber Bragg grating-based temperature sensing. *IEEE Photon Technol. Lett.* **31**, 939–942 (2019).
24. Choi, B. K. et al. Simultaneous temperature and strain measurement in fiber Bragg grating via wavelength-swept laser and machine learning. *IEEE Sens. J.* **24**, 27516–27524 (2024).
25. Manavi Roodsari, S. et al. Shape sensing of optical fiber Bragg gratings based on deep learning. *Mach. Learn. : Sci. Technol.* **4**, 025037 (2023).
26. Fasseaux, H., Loyez, M. & Caucheteur, C. Machine learning unveils surface refractive index dynamics in comb-like plasmonic optical fiber biosensors. *Commun. Eng.* **3**, 34 (2024).
27. Chubchev, E. D. et al. Machine learning approach to data processing of TFBG-assisted SPR sensors. *J. Lightwave Technol.* **40**, 3046–3054 (2022).
28. Liu, Z. et al. Deep learning assisted real-time and portable refractometer using a π-phase-shifted Tilted fiber Bragg grating sensor. *Photonics Res.* **13**, 2202–2212 (2025).
29. Feng, T. et al. Distributed transverse-force sensing along a single-mode fiber using polarization-analyzing OFDR. *Opt. Express*. **28**, 31253–31270 (2020).
30. Ye, Z. et al. Fiber Bragg grating sensors demodulated by a speckle silicon chip. *Opt. Lett.* **50**, 2302–2305 (2025).
31. Liu, H. et al. Multi-angle fiber Bragg grating (FBG) – transverse strain system for deep shear displacement measurement. *Measurement* **258**, 119398 (2026).
32. Akiba, T. et al. Optuna: A next-generation hyperparameter optimization framework. *Proc. of the 25th ACM SIGKDD international conference on knowledge discovery & data mining* 2623–2631 (2019).

Author contributions

V. T. conducted the experiments and the data analysis. He drafted the manuscript.B. V. assisted V. Tocanne in the analysis and co-wrote the manuscript.D. K. fabricated the FBGs, revised the experiments and the manuscript.C. G. supervised the work and revised the manuscript.C. C. supervised the work and co-wrote the manuscript.

Funding

Christophe Caucheteur is supported by the Fonds de la Recherche Scientifique (F.R.S.-FNRS), under Research Director Position.

Declarations

Competing interests
The authors declare no competing interests.

Additional information
Correspondence and requests for materials should be addressed to B.E.

Reprints and permissions information is available at www.nature.com/reprints.

Publisher's note Springer Nature remains neutral with regard to jurisdictional claims in published maps and institutional affiliations.